

Measurement of the associated production of a Z boson and bottom or charm quarks with the ATLAS experiment

Jacob Oliver

June 28, 2019

Abstract

This document presents the first step in obtaining unfolded cross sections of the $Z \rightarrow (\mu\mu) + b$ and $Z \rightarrow (\mu\mu) + bb$ channels, in addition to measurements of kinematic variables. The analysis uses data collected by the ATLAS experiment at the LHC of p-p collisions corresponding to 80fb^{-1} at a centre of mass energy of $\sqrt{s} = 13\text{ TeV}$. The benefits of a measurement of unfolded cross sections of kinematic variables for these processes are briefly discussed before the presentation of the measurement results. The plots show a good modelling of data by the Monte Carlo simulation, and provide an adequate starting point for later analysis and unfolding of these cross sections.

Contents

1	Introduction	1
2	Physical Theory	3
2.1	The Standard Model	3
2.2	Describing the Standard Model Mathematically	6
2.2.1	Quantum Chromodynamics	6
2.2.2	Electroweak Theory	7
2.2.3	Higgs Mechanism	8
2.3	Signal Processes	10
2.4	Background Processes	12
3	LHC and ATLAS	15
3.1	LHC	15
3.2	ATLAS	15
3.2.1	Magnet System	16
3.2.2	Inner Detector	17
3.2.3	Calorimeter System	19
3.2.4	Muon System	22
3.2.5	Trigger System	24

1 Introduction

The production of a Z boson from p-p collisions is an ideal target for analysis due to the strong identifiers of the process. The clear experimental signature of a Z boson decaying to two muons is combined with the long lifetimes of b-hadrons to create a signature which is easy to observe, and that provides an excellent opportunity to study the production and dynamics of heavy flavour physics (heavy flavour physics is physics pertaining to quarks at the heavier end of the scale, namely bottom and charm, but not top quarks which have their own area of study).

In the Standard Model (SM), there are multiple processes which create the signal source of Z boson production in association with two b quarks, with the Z boson later decaying to two muons. While these processes occur via different mechanisms, they all arrive at the same final state which this analysis examines. Each of these processes occurs via the strong interaction, the most common of which is the radiation of a gluon which splits into a bb pair. This is one of the central motivations to measuring $Z \rightarrow (\mu\mu) + bb$ processes: performing a measurement of the strong signal processes allows the investigation of QCD phenomena and strong coupling coefficients, which could potentially lead to a more precise SM in the future.

Current heavy flavour cross sections are calculated using next-to-leading-order perturbative quantum chromodynamics (NLO pQCD), and are associated with large theoretical uncertainties [1]. Cross sections of heavy flavour + jet interactions have been available for some time [2–4]. These processes have already been measured at lower centre of mass energy by both ATLAS [5] and CMS [6], however by performing a measurement of these cross sections at higher energies it can be tested that the NLO pQCD calculations hold and help to constrain the theoretical uncertainties.

Currently NLO pQCD calculations involving heavy flavour are associated with one of two schemes named the four-flavour number scheme (4FNS) and five-flavour number scheme (5FNS). In the 4FNS b quarks appear only in the final state of a given process, and are considered to be massive (i.e. only the parton densities of gluons and the first two quark generations are considered within the proton). In the 5FNS, the presence of an additional b quark density is allowed within the initial state [7].

By definition these schemes must always give identical results if contributions from all orders are added, however the manner of ordering the perturbative expansion is not consistent between the two schemes at any given order. This allows the possibility of a difference between the two schemes to arise, however this can occur when the schemes are considered at a fixed order. There are advantages and disadvantages to each of the schemes [8], and this analysis allows an insight into both the 4FNS and 5FNS.

The $Z \rightarrow (\mu\mu) + bb$ process follows the 4FNS scheme as there are multiple mechanisms which allow for the production of a b quark pair in the final state, whereas the $Z \rightarrow (\mu\mu) + b$ process must follow the 5FNS scheme in order for an individual b quark to be present in

the final state. As such, the $Z \rightarrow (\mu\mu) + b$ process allows for a b-quark density in the initial state. It is possible for quark-antiquark pairs with short lifetimes to be produced within the protons of the Large Hadron Collider (LHC) as quantum fluctuations from gluons. The quarks produced in these fluctuations are referred to as sea-quarks, and can interact with other present partons when the protons collide.

Analysis of the individual b quarks present in the final state of $Z \rightarrow (\mu\mu)$ presents an opportunity to better understand of the structure of the 5FNS and the proton Parton Distribution Function (PDF) [9], which could also potentially lead to improvements in the understanding of the SM.

Another benefit of performing a measurement of this process comes when considering its relation to other physical processes. The final state of two muons and two b quarks is not uncommon, and many other processes have similar final states which leads to $Z \rightarrow (\mu\mu) + bb$ being a common background. Many processes across multiple physical areas share this background, such as Higgs processes, and Dark Matter and SUSY searches. By obtaining a detailed measurement of $Z \rightarrow (\mu\mu) + bb$ production, it is possible to improve the precision of many searches with similar final states.

There are, however, difficulties in performing a measurement such as this. Just as $Z \rightarrow (\mu\mu) + bb$ provides a background for many physical searches due to the shared final state, there are many additional background processes to $Z \rightarrow (\mu\mu) + bb$. This makes a direct measurement difficult; an informed understanding of the background processes involved is essential in order to perform a good measurement.

The following report outlines and explains the steps used to perform a measurement of these processes using data collected by ATLAS at the LHC.

2 Physical Theory

2.1 The Standard Model

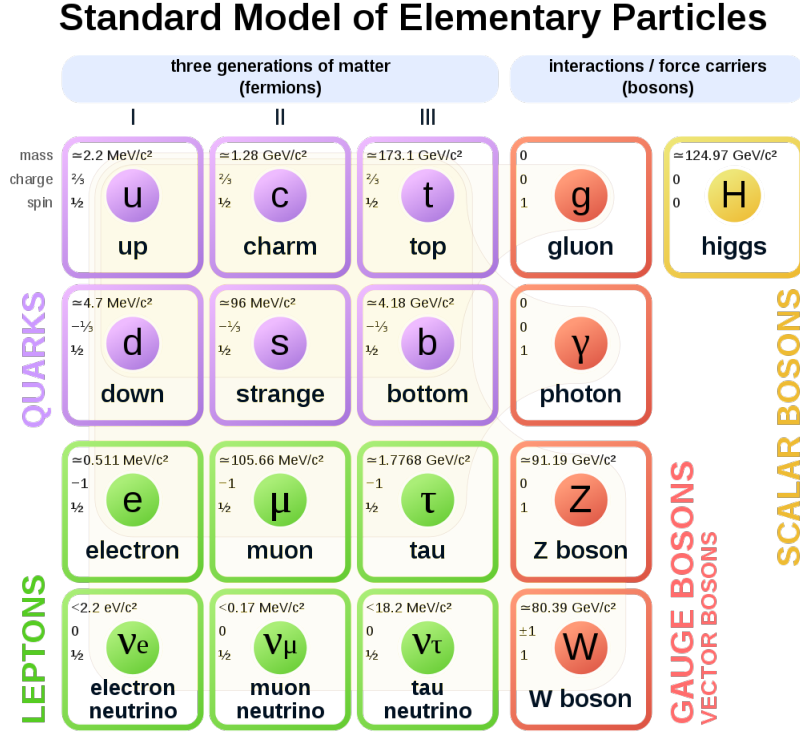


Figure 2.1: The Standard Model of particle physics.

To study particle physics is to study the fundamental constituents of matter, and the interactions between them. In order to describe both these constituents and the interactions between them, a model called the Standard Model (SM) is used. The SM is a local, Lorentz-invariant quantum field theory. These interactions arise from the requirement of local gauge invariance within the SM, and can be described by group theory. The SM gauge group is as follows:

$$SU(3)_C \otimes SU(2)_L \otimes U(1)_Y \quad (1)$$

where C is colour, L is left-handedness, and Y is hypercharge. In the SM, constituent matter particles are titled *fermions*: half integer spin particles that obey Fermi Dirac statistics. The forces that cause the interactions between fermions are described by *gauge*

Gauge Boson	Mass	Charge	Spin	Force	Theory
gluon	0	0	1	strong	QCD
W^\pm	80.379 ± 0.012	± 1	1	weak	Electroweak
Z^0	91.1876 ± 0.0021	± 1	1	weak	Electroweak
γ	$< 1 \times 10^{-18}$	0	1	electromagnetic	Electroweak

Table 2.1: A table showing the properties of the Standard Model gauge bosons[7].

bosons: integer spin particles that obey Bose Einstein statistics. Each force is carried by a particular type of these mediator bosons: photons (γ) carry the electromagnetic force, gluons (g) carry the strong force, and W^\pm and Z^0 bosons carry the weak force. Gravity is the only known fundamental force that is not described by the SM. Table 2.1 summarises the properties of the SM bosons.

Fermions can be further subsectioned into two separate groups: quarks and leptons. Each group has three generations which, as a general rule of thumb, have increasing particle mass from generation to generation.

Leptons are classified by their charge (Q), lepton flavour number (the lepton flavour number is different for each generation of lepton and can be electron number (L_e), muon number (L_μ), or tau number (L_τ)), and the third component of weak isospin (T_3). It is also important to consider the additional quantity of weak hypercharge (Y_W) which is directly related to both the lepton charge and weak isospin by the equation:

$$Y_W = 2 \cdot (Q - T_3) \quad (2)$$

The charged leptons (i.e. e , μ , and τ) are able to interact via both the weak and the electromagnetic force, however the neutral leptons (ν_e , ν_μ , and ν_τ) can only interact with the weak force. Table 2.2 summarises the properties of leptons within the SM.

For each lepton a left-handed weak isospin doublet is formed:

$$\begin{pmatrix} T_3 = +1/2 \\ T_3 = -1/2 \end{pmatrix} = \begin{pmatrix} \nu_{eL} \\ e_L^- \end{pmatrix}, \begin{pmatrix} \nu_{\mu L} \\ \mu_L^- \end{pmatrix}, \begin{pmatrix} \nu_{\tau L} \\ \tau_L^- \end{pmatrix} \quad (3)$$

The SM forbids right-handed neutrinos, and as such weak isospin singlets ($T_3 = 0$) are formed by the right handed leptons in each generation: e_R^- , μ_R^- , and τ_R^- .

Quarks are classified by their charge (Q), and their flavour quantum numbers: baryon number (the third component of the isospin (I_3)), strangeness (S), charmness (C), bottomness (B), and topness (T). Unlike the SM bosons and leptons, quarks are able to

Lepton Flavour	Mass	Q	Y_W	L_e	L_μ	L_τ
e^-	0.511 MeV	-1	-1	1	0	0
ν_e	< 2 eV	0	-1	1	0	0
μ	105.7 MeV	-1	-1	0	1	0
ν_μ	< 0.19 MeV	0	-1	0	1	0
τ	1776.8 MeV	-1	-1	0	0	1
ν_τ	< 18.2 MeV	-1	-1	0	0	1

Table 2.2: A table showing the properties of the Standard Model leptons[7].

Quark Flavour	Mass	Q	I_3	C	S	T	B
u	$2.3^{+0.7}_{-0.5}$ MeV	2/3	1/2	0	0	0	0
d	$4.8^{+0.7}_{-0.3}$ MeV	-1/3	-1/2	0	0	0	0
c	1.275 ± 0.025 GeV	2/3	0	1	0	0	0
s	95 ± 5 MeV	-1/3	0	0	-1	0	0
t	173.2 ± 0.9 GeV	2/3	0	0	0	1	0
b	4.18 ± 0.03 GeV	-1/3	0	0	0	0	-1

Table 2.3: A table showing the properties and quantum numbers of the SM quarks[7].

interact via all three of the fundamental forces. In addition to these flavour quantum numbers, quarks also have an additional quantum number named colour charge which can take one of three values (often referred to as red, blue, or green). The term colour only describes this quantum numbers, as quarks do not have a "non-physical" colour. Table 2.3 summarises the properties of the SM quarks.

In addition to the quarks and leptons, each fermion has its own antiparticle. These antiparticles are opposites to their matter particles, with reversed signs for all quantum numbers. We can obtain the total number of fermions in the standard model by simply summing their number: 6 leptons, 6 antileptons, 18 quarks (there are three variations for each quark flavour due to the three colour charges), and 18 antiquarks. This gives the SM a total of 12 leptons and 36 quarks.

The SM is a highly successful model and the predictions of the models have been tested to very high levels of accuracy by CERN, however it is known that the model is imperfect (hence the need for experimental physics). In order to improve the model, it must be rigorously tested in every facet until it is broken (such that it can then be revised and improved).

An example of this process can be seen by considering the constraint placed on the SM by electroweak (EW) theory: under EW theory, the masses of the W^\pm and Z^0 bosons (i.e.

the gauge bosons of the weak force) violate invariance under local gauge transformations. However, despite this the W^\pm and Z^0 bosons have large masses. In order to account for this within the SM, the Higgs mechanism is required. The Higgs mechanism results in the presence of an additional gauge boson with a mass of 125 GeV in the SM known as the Higgs boson [10][11]. The Higgs mechanism is described in greater detail in section 2.2.3.

2.2 Describing the Standard Model Mathematically

2.2.1 Quantum Chromodynamics

The strong interaction is driven by a process known as Quantum Chromodynamics (QCD)[7][12]: a non-Abelian gauge theory based on the SU(3) symmetry group of colour. This group has eight generators which correspond to the eight massless gluons that mediate the interactions of coloured quarks. These quarks are described by colour triplets:

$$q_f^T = (q_f^1, q_f^2, q_f^3) \quad (4)$$

with 1, 2, and 3 representing the three colour states of red, green, and blue. The Lagrangian density of QCD is given by

$$L_{QCD} = \sum_{j=1}^{n_f} \bar{q}_j (iD_\mu \gamma^\mu - m_j) q_j - \frac{1}{4} \sum_{A=1}^8 F^{A\mu\nu} F_{\mu\nu}^A \quad (5)$$

The first sum of this equation corresponds to the quark contribution, and the second the gluon contribution. This equation is written with the quark-field spinors, q_j , and the quark masses m_j . $D_\mu = \partial_\mu - ig_s T_A \mathcal{A}_\mu^A$ is the covariant derivative, where \mathcal{A}_μ^A correspond to the gluon fields and T_A to the eight generators of the SU(3) symmetry group. The γ^μ represent the Dirac matrices and $F_{\mu\nu}^A$ represents the field strength tensor based on the gluon field \mathcal{A}_μ^A

$$F_{\mu\nu}^A = \partial_\mu \mathcal{A}_\nu^A - \partial_\nu \mathcal{A}_\mu^A - g_s f_{ABC} \mathcal{A}_\mu^B \mathcal{A}_\nu^C \quad (6)$$

with the QCD coupling constant, $g_s = \sqrt{4\pi\alpha_s}$, and the structure constants of the SU(3) symmetry group.

The SU(3) group is a non-Abelian group and as such the third term in Eq. 6 does not vanish and thus the present gluon fields are able to self-interact. The self interaction leads to asymptotic freedom as the effective coupling constant of the strong interaction decreases with increasing energy. In this case, quarks and gluons can be treated as free and their interactions can be calculated within perturbative theory (for short distances where the strong coupling constant converges asymptotically against zero). However, with increasing distance between two quarks, the quarks become bounded in hadrons through a process called confinement.

2.2.2 Electroweak Theory

The electroweak (EW) theory is the gauge theory behind the electroweak force. The electromagnetic and weak interactions can be unified under the $SU(2)_L \otimes U(1)_Y$ symmetry group, and this is described by EW theory. The SU(2) group involves three gauge fields with a corresponding gauge bosons of W_μ^i with $i = 1, 2, 3$. The U(1) group involves a single gauge field and a corresponding gauge boson of B_μ . The Lagrangian of EW theory is

$$\mathcal{L}_{EW} = \sum_{j=1}^3 i\bar{\psi}_j(x)\gamma^\mu D_\mu \psi_j(x) - \frac{1}{4}B_{\mu\nu}B^{\mu\nu} - \frac{1}{4}W_{\mu\nu}^j W_j^{\mu\nu} \quad (7)$$

with $\sum_{j=1}^3 i\bar{\psi}_j(x)\gamma^\mu D_\mu \psi_j(x)$ corresponding to the fermion contribution and the remainder of the equation corresponding to the contribution from the gauge field. In this equation, D_μ describes the covariant derivative

$$D_\mu = \partial_\mu - ig\frac{\sigma_j}{2}W_\mu^j(x) - ig'\frac{Y}{2}B_\mu(x) \quad (8)$$

with the coupling constants g and g' corresponding to $SU(2)_L$ and $U(1)_Y$ respectively. The fermionic half of the equation contains a term corresponding to the kinetic energy of the fermions along with the a covariant derivative term which describes the interaction of fermions with the gauge field. No explicit mass term for the fermions is allowed in this Lagrangian as such a term would result in a mixture of left-handed multiplets and right-handed singlets. As the weak interaction can only couple to left-handed fermions, this would require a violation of local gauge invariance which is forbidden.

Similarly to the fermionic half of the equation, the gauge field portion of the equation contains a term for kinetic energy and a term for the self interaction between the gauge

fields. In order to avoid violation of the invariance of local gauge transformations, this portion of the Lagrangian also excludes any explicit mass term.

The four gauge bosons resultant of the $SU(2)_L \otimes U(1)_Y$ symmetry group do not directly translate into the SM bosons of W^\pm , Z , and γ . W^\pm are linear combinations of W_μ^1 and W_μ^2

$$W_\mu^\pm = \frac{1}{\sqrt{2}}(W_\mu^1 \mp iW_\mu^2) \quad (9)$$

which represent the charged part of the interaction. Z and γ represent the neutral part of the interaction and evolve from the mixing of the W_μ^3 and B_μ neutral fields

$$\begin{pmatrix} A_\mu \\ Z_\mu \end{pmatrix} = \begin{pmatrix} \cos \theta_W & \sin \theta_W \\ -\sin \theta_W & \cos \theta_W \end{pmatrix} \begin{pmatrix} B_\mu \\ W_\mu^3 \end{pmatrix} \quad (10)$$

with the weak mixing angle θ_W .

2.2.3 Higgs Mechanism

The presence of the massive W^\pm and Z bosons within EW theory requires that these masses be accommodated in a gauge invariant and renormalisable manner: the Higgs mechanism [13][14].

In the Higgs mechanism, the spontaneous symmetry breaking of the quantum vacuum ground state generates the masses of the W^\pm and Z bosons while leaving the fundamental symmetry of EW theory unchanged. The Higgs mechanism introduces a complex scalar $SU(2)$ doublet ϕ with a hypercharge $Y = 1$

$$\phi(x) = \begin{pmatrix} \phi^{(+)}(x) \\ \phi^0(x) \end{pmatrix} = \sqrt{\frac{1}{2}} \begin{pmatrix} \phi_1(x) + i\phi_2(x) \\ \phi_3(x) + i\phi_4(x) \end{pmatrix} \quad (11)$$

Coupling ϕ to the gauge bosons allows a gauge invariant Lagrangian to be obtained:

$$L_{Higgs} = (D_\mu \phi)^\dagger D^\mu \phi - V(\phi) \quad (12)$$

using the covariant derivative D_μ defined in Eq 8. $V(\phi)$ describes the most general renormalisable potential invariant under an $SU(2)_L \otimes U(1)_Y$ gauge transformation

$$V(\phi) = \mu^2 \phi^\dagger \phi + \lambda (\phi^\dagger \phi)^2 \quad (13)$$

The potential is dependent upon the choice of μ and λ , as this selection constrains the bounds of the potential. In the instance where $\mu^2 < 0$ and $\lambda > 0$ the potential is bounded from below, and has a rotationally symmetric degenerate ground state

$$-\frac{\mu^2}{2\lambda} = \frac{v^2}{2} \quad (14)$$

where v describes the vacuum expectation value related to the Fermi constant G_F

$$v = \sqrt{\frac{1}{\sqrt{2}G_F}} \approx 246.22 \text{ GeV} \quad (15)$$

$\phi(x)$ is expanded using Eq. 12 via perturbation theory. The ground state can be fixed to $\phi_1 = \phi_2 = \phi_4 = 0$ and $\phi_3 = v$ at

$$\phi_0(x) = \frac{1}{\sqrt{2}} \begin{pmatrix} 0 \\ v \end{pmatrix} \quad (16)$$

as the choice of ground state is arbitrary when considering a rotation in phase space. The ground state is invariant with respect to a $U(1)_{em}$ symmetry (which is a subgroup of $SU(2)_L \otimes U(1)_Y$). The Higgs $SU(2)$ doublet can be further expanded around the ground state $\phi_0(x)$, which results in

$$\phi(X) = \frac{1}{\sqrt{2}} \begin{pmatrix} 0 \\ v + H(X) \end{pmatrix} \quad (17)$$

Once the vacuum state of Eq. 14 is chosen, the underlying symmetry of $SU(2)_L \otimes U(1)_Y$ is spontaneously broken. The photon is left massless due to the remaining symmetry of $U(1)_{em}$. Three of the four degrees of freedom of EW theory are absorbed by the longitudinal polarization of the gauge bosons to form the massive W^\pm and Z^0 bosons. The remaining degree of freedom corresponds to the Higgs boson - a neutral scalar particle.

In summary, the above equations give the following Lagrangian for the Higgs field after spontaneous symmetry breaking has occurred:

$$\begin{aligned}
L_{Higgs} = & \frac{1}{2} \partial_\mu H \partial^\mu H + \text{const} \\
& + \frac{1}{4} g^2 v^2 W_\mu^+ W^{-\mu} + \frac{1}{8} (g'' + g'^2) v^2 Z_\mu Z^\mu - \lambda v^2 H^2 \\
& + \frac{1}{2} g^2 v H W_\mu^+ W^{-\mu} + \frac{1}{4} (g^2 + g'') v H Z_\mu Z^\mu \\
& + \frac{1}{4} g^2 H^2 W_\mu^+ W^{-\mu} + \frac{1}{8} (g^2 + g'^2) H^2 Z_\mu Z^\mu \\
& - \lambda v H^3 - \frac{1}{4} \lambda H^4
\end{aligned} \tag{18}$$

For each of the gauge bosons at tree level, a mass term can be determined directly from the Lagrangian

$$M_W = \frac{1}{2} v g = \frac{ev}{2 \sin \theta_W} \tag{19}$$

$$M_Z = \frac{1}{2} \sqrt{g^2 + g'^2} v = \frac{ev}{2 \sin \theta_W \cos \theta_W} = \frac{M_W}{\cos \theta_W} \tag{20}$$

$$M_\gamma = 0 \tag{21}$$

$$M_H = v \sqrt{2\lambda} \tag{22}$$

$$\tag{23}$$

The vacuum expectation value is a direct factor of both the W and Z mass, hence it could be determined by measuring the masses of both bosons. The Higgs boson, however, cannot be calculated from the vacuum expectation value due to its dependence on λ which is a free parameter in the SM.

Fermion mass terms must be added via trilinear Yukawa couplings of the fermions to the Higgs fields, and this results in additional terms for the Lagrangian. These fermion masses are given by

$$m_f = \frac{1}{\sqrt{2}} g_f v \tag{24}$$

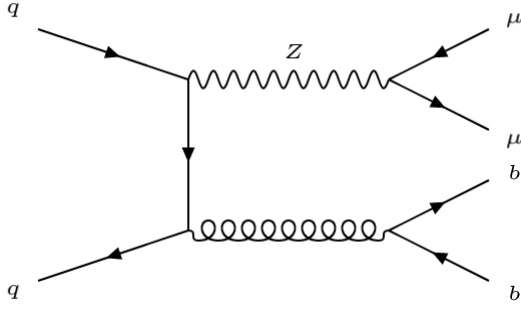
with the coupling constants g_f being free parameters of the SM.

2.3 Signal Processes

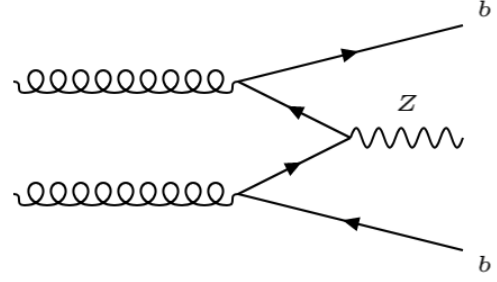
The most common production of a Z boson which decays to two muons is through the Drell-Yan process [15] - a quark-antiquark pair from two colliding protons annihilate and

produce two muons through the weak force mediated by a Z boson. However, in order to arrive at the final state either of the signal processes for this analysis ($Z \rightarrow (\mu\mu) + b$ or $Z \rightarrow (\mu\mu) + b\bar{b}$), an additional requirement must be met - the presence of one or two b-quarks.

The most common mechanism for this process to occur is for one of the annihilating quarks to radiate a gluon. The gluon then produces a pair of b-quarks (with one a standard b-quark, and the other an anti b-quark), meeting the requirements for the final state of the process. The Feynman diagram of this process can be seen in Figure 2.2a.



(a) $q\bar{q}$ annihilation in conjunction with the radiation of a gluon.



(b) The final state produced by interactions of a gluon pair.

Figure 2.2: A figure showing two possible mechanisms by which a $Z \rightarrow (\mu\mu) + b\bar{b}$ final state can be achieved.

Another dominant process for this production is a pair of gluons producing two quark-antiquark pairs. Each of the two gluons produces a $b\bar{b}$ pair, and interaction between the two pairs allows two of the quarks to annihilate and produce a Z boson (which later decays to two muons). The Feynman diagram for this process can be seen in Figure 2.2b.

Finally, another process to be considered is that of the Compton process by which the interaction of a gluon with a single quark radiates a Z boson. It is this process that allows for the insight into the structure of the proton. At any one time, the content of a proton can be described by its PDF.

The PDF of a given parton is a function of two variables: the fraction of the proton momentum carried by a parton (x), and the "scale" corresponding to the energy at which the parton is probed (Q^2). As the protons are collided inside the LHC beamline, the sea-quarks within the proton are able to interact with other partons such as gluons. For example in the case of $Z \rightarrow (\mu\mu) + b$, the gluons and quarks interact via a hard process to produce a final state with one b-quark and a Z boson, which is subsequently detected by ATLAS. The cross section for this hard process can be written in the following form:

$$\sigma(qg \rightarrow Zq) = \Sigma C_i^P(x, \alpha_s(Q^2)) \otimes \tilde{f}_i(x, Q^2, \alpha_s(Q^2)) \quad (25)$$

With $C_i^P(x, \alpha_s(Q^2))$ as the perturbative calculable coefficient function, and $f_i(x, Q^2, \alpha_s(Q^2))$ the probability to find a parton of type i carrying a fraction x of the proton momentum and $\tilde{f}_i(x, Q^2, \alpha_s(Q^2)) = x f_i(x, Q^2, \alpha_s(Q^2))$ [16]. When the process is detected, the momentum of the incident quarks can be calculated and used to perform a measurement of the proton PDF. PDFs are useful for calculating the cross sections of physical processes, and a measurement of $Z \rightarrow (\mu\mu) + b$ allows for a measurement of the proton PDF as well. The Feynman diagram for this process can be seen in Figure 2.3.

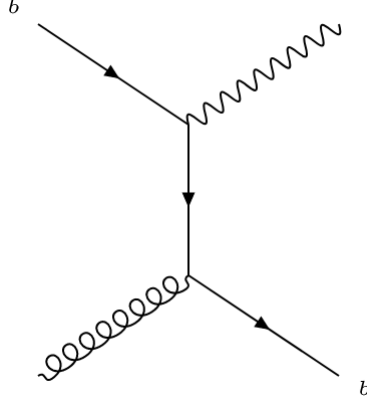


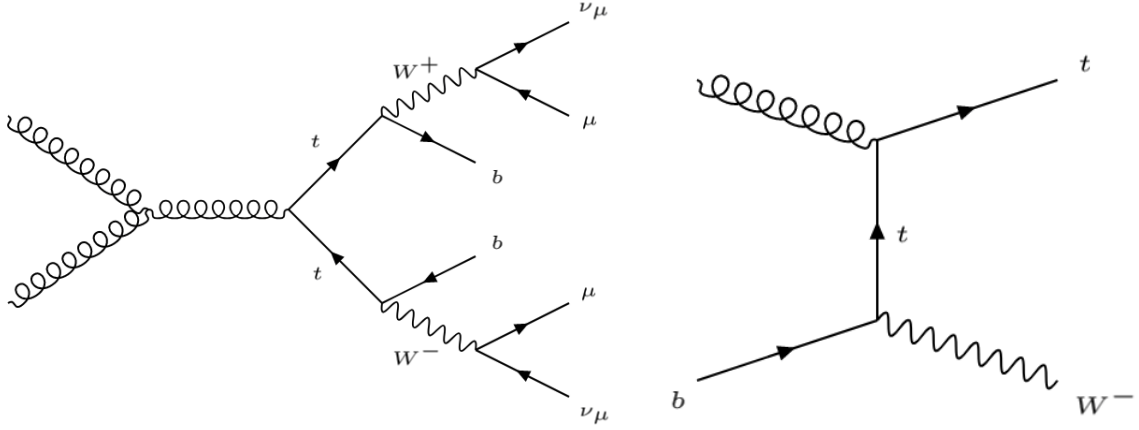
Figure 2.3: A figure showing the Feynman diagram for the Compton Process.

2.4 Background Processes

The difficulty of $Z \rightarrow (\mu\mu) + bb$ analysis is in no small part due to the number of background processes that make a direct measurement difficult. In order to obtain a clear and accurate measurement of the signal process, there must be an equally clear understanding of the background processes such that any effect they have on a measurement of the signal process can be modelled and removed.

The first and most common of these background processes is the top quark pair background. A pair of top quarks (specifically $t\bar{t}$) are produced through one of many potential mechanisms, such as via a gluon interaction. Each top quark then undergoes a flavour change to become a b quark, and produces a muon via a W boson and weak decay (as the overall charge of the process must be conserved). This results in the same final state as the $Z \rightarrow (\mu\mu) + bb$ signal process plus two additional neutrinos from the flavour change of each top quark to a bottom quark. The Feynman diagram for this process can be seen in Figure 2.4a.

Another background process dependent on a charged current interaction is the single top background process. An incoming b-quark interacts with a gluon and experiences a flavour change. A W boson is produced alongside a top quark, corresponding to the flavour change of the b-quark. This results in the emission of only a single top quark,



(a) The Top Quark Pair Production background process. (b) The Single Top background process.

Figure 2.4: A figure showing the Feynman diagrams of Top Quark Pair Production and Single Top background production.

along with a W boson. This process can be seen in Figure 2.4b. The final state is achieved by the flavour change of first the top quark, which produces the necessary b -quark and an additional W boson, followed by the leptonic decay of two W bosons which produce a muon and a neutrino each.

In addition to these background processes are the diboson background processes. In these interactions, annihilating quarks produce a combination of two bosons which produce the required final state particles. The first of these processes is referred to as $ZqqZll$, in which both of the bosons produced are Z bosons. One Z boson decays to two leptons, and the second decays to two quarks. The most common source of this background in $Z \rightarrow (\mu\mu) + b\bar{b}$ production is the case where one Z boson decays to two muons, and the other to two b -quarks. This process can be seen in Figure 2.5a.

The second of these diboson processes is referred to as $WqqZll$. This process is similar to the $ZqqZll$ process, however in this instance only one of the produced bosons is a Z boson and the other is a W boson (as opposed to both being Z bosons). In this case, the W boson decays to two quarks, and the Z boson to two leptons. The most common form that this background process takes in the $Z \rightarrow (\mu\mu) + b\bar{b}$ analysis is the case where the W boson decays to a bottom quark and a charm quark, and the Z boson decays to produce two muons. This immediately fulfils the final state of the $Z \rightarrow (\mu\mu) + b\bar{b}$ processes, and can easily imitate the $Z \rightarrow (\mu\mu) + b\bar{b}$ process if the charm quark is mistagged as a b -quark. These background processes ($WqqZll$ and $ZqqZll$) are a small yet common background that is consistently present across the full energy range of the analysis. The Feynman diagram for these processes can be seen in Figure 2.5.

In addition to the $WqqZll$ and $ZqqZll$ backgrounds mentioned above, there is an additional

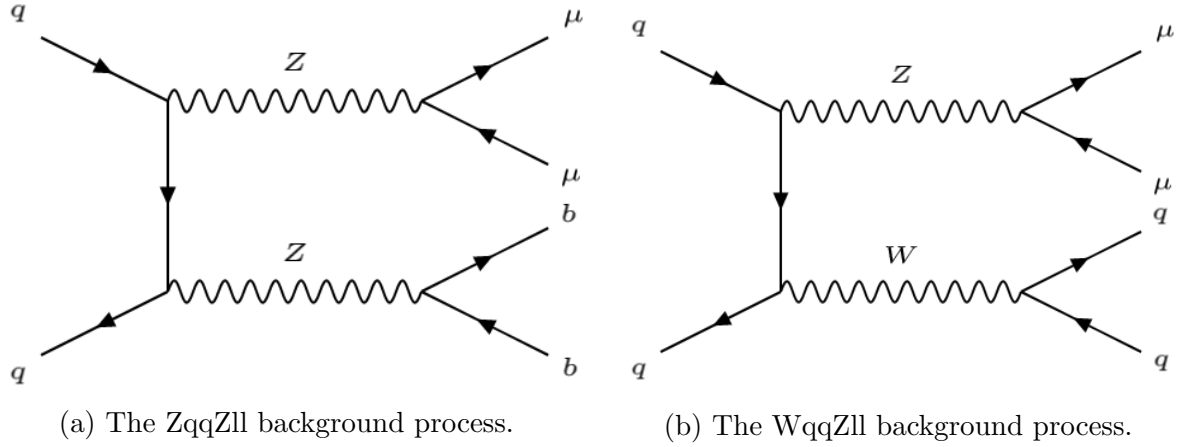


Figure 2.5: A figure showing the Feynman diagrams for the WqqZll and ZqqZll background processes.

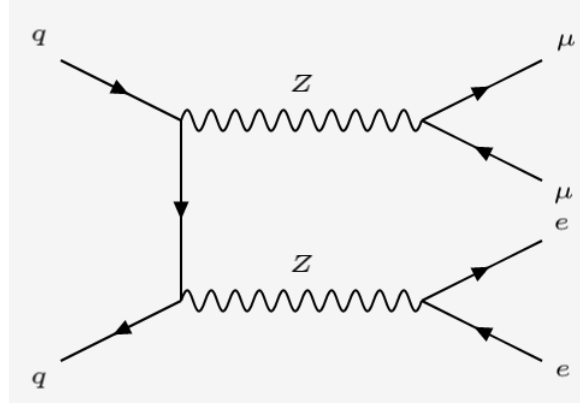


Figure 2.6: The ZZ4l background process.

background process named ZZ4l which corresponds to an event where the two produced Z bosons decay into four leptons. The Feynman diagram for this process can be seen in Figure 2.6. This background process occurs when one of the Z bosons produces two muons, and the other two electrons. Electrons produce jets along with electromagnetic showers within the electromagnetic calorimeters in ATLAS (see section 3.2.3), and a background process is found where this reconstructed jet is mistagged as a b-jet.

3 LHC and ATLAS

3.1 LHC

The Large Hadron Collider (LHC) [17] is a 26.7km particle accelerator and collider. Nearing completion of its second run of its data collection (appropriately named Run 2) the LHC collides particle bunches of up to 10^{11} particles at a centre of mass energy $\sqrt{s} = 13$ TeV 40 million times each second in order to achieve a design luminosity of $10^{34}\text{cm}^{-2}\text{s}^{-1}$. The protons are sourced from hydrogen atoms in a bottle of gas - the hydrogen is passed through an electric field to strip away its electrons, and the resulting protons are then accelerated through a series of smaller accelerators to increase their energy to desired levels.

The protons are accelerated to 50 MeV by LINAC 2, up to 1.4 GeV by the Proton Synchrotron Booster (PSB), then to 25 GeV by the Proton Synchrotron (PS). The final step before the protons are injected into the main LHC pipes is an acceleration to 450 GeV by the Super Proton Synchrotron (SPS). The protons are injected evenly into each of the two LHC beam pipes where they are accelerated in opposite directions to their maximum energy of 6.5 TeV [17]. Each of these accelerators can be seen in Figure 3.1.

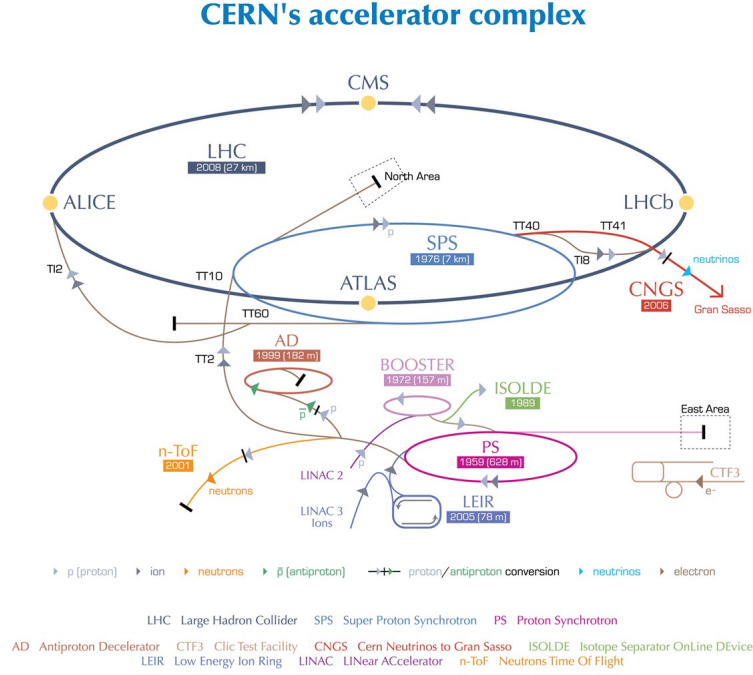
Once the protons have reached their maximum energy, they are focussed and collided at one of the four interaction points around the circumference of the LHC ring. The collisions that produce the data used in this analysis occur at Point 1: The ATLAS detector [17].

3.2 ATLAS

The ATLAS (A Toroidal LHC ApparatuS) experiment [19–21] is one of the larger detectors in place along the circumference of the LHC beam pipe. ATLAS is a general purpose detector, and has been carefully engineered to maximise its potential in the probing of p-p collisions at the LHC.

ATLAS and its components are described in a specific coordinate system using the interaction point and axis of the proton beam as a reference: The nominal interaction point (IP) is defined as the origin of the coordinate system, and the direction of the beam axis is defined as the positive z-axis. In addition to this, the positive y-axis is defined as pointing vertically upwards in relation to the IP, and the positive x-axis as pointing horizontally from the IP to the centre of the LHC ring. This automatically defines the x-y plane to be the plane tangential to the direction of the beam axis (z-axis).

In this coordinate system, cylindrical coordinates are used to parametrise the geometry within the detector: the polar angle θ is the angle from the beam axis and the azimuthal angle ϕ is the angle around the beam direction in the x-y plane. The pseudorapidity is then defined in terms of θ as $\eta = -\ln[\tan(\theta/2)]$. Using this, the distance between two



European Organization for Nuclear Research | Organisation européenne pour la recherche nucléaire

© CERN 2008

Figure 3.1: A figure showing the rings of the CERN accelerator complex [18].

points in $\eta - \phi$ space can be defined as $\Delta R = \sqrt{\Delta\eta^2 + \Delta\phi^2}$.

In order to maximise the acceptance in pseudorapidity and cover the largest azimuthal angle possible (i.e. to maximise detection coverage of any events that occur within the detector), ATLAS is symmetrical with respect to the path of the accelerated protons. The ATLAS detector operates using a combination of several subsystems, each of which can be seen in Figure 3.2.

These subsystems are layered outwards from the central interaction points, largely in the form of concentric cylinders (however this is not true for every component which will be discussed in the following sections). These systems can be organised into four categories based on their function: the magnet system, the inner detector, the calorimeter system, and the muon system. Together with the trigger system, these components are designed to allow ATLAS to operate with the highest possible efficiency.

3.2.1 Magnet System

The ATLAS magnet system consists of four magnets: a single solenoid magnet, and three toroidal magnets (which contribute an important part of the ATLAS name). The central solenoid provides the magnetic field for the inner detector, and the toroidal magnets

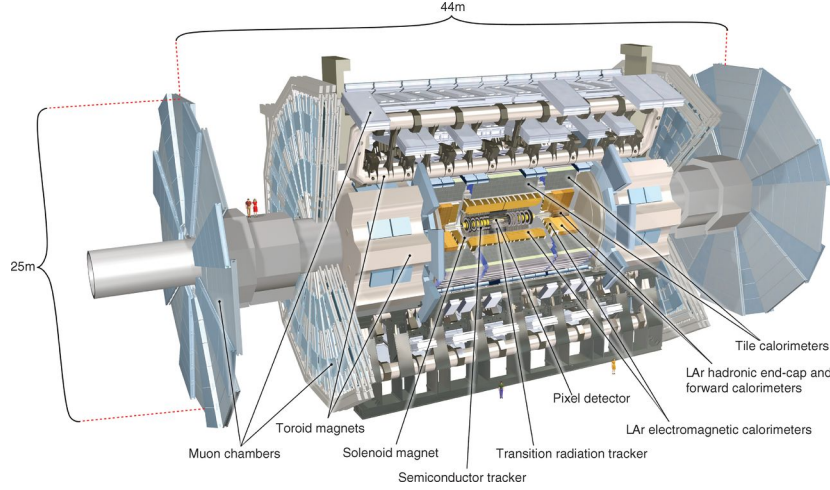


Figure 3.2: A figure showing the subsystems of the ATLAS detector [21].

provide the magnetic field for the muon system.

The solenoid magnet is named the Central Solenoid Magnet and serves the purpose of bending the path of charged particles within the inner detector so that their momentum may be measured. The most important function of this system for this analysis is the 2T axial magnetic field that it exerts within ATLAS. The magnet weighs 5 tonnes, and is aligned with the z-axis of the beam pipe. The solenoid magnet is also capable of storing a total of 38MJ of energy.

The toroidal magnets have different designs for their varying purposes. The first is the end-cap magnets: large, doughnut shaped magnets that rest at either end of the detector and provide the magnetic field in the end-cap regions of the muon system. The second is the barrel toroid - longer, 25.3m toroidal coils that span the length of the muon system and provide a constant toroidal magnetic field to that system. The contributions of the barrel and end-cap toroids to the toroidal field around the muon detectors is as follows: 0.5T from the barrel toroid, and 1T from each of the end-cap toroids. Each end-cap magnet weighs 240 tonnes and stores 0.25GJ of energy. The barrel toroid consists of eight individual coils stored within vacuum vessels that surround both the end-cap magnets and the calorimeter systems. The barrel toroid weighs a total of 830 tonnes, and stores a total of 1.08GJ of energy. The shape of the ATLAS magnetic field can be seen in Figure 3.3. [19–21]

3.2.2 Inner Detector

The inner detector is the most central component of ATLAS and makes the most immediate measurements after a collision such as those of the primary and secondary vertex, and of particle momentum. The inner detector covers a pseudorapidity range of $|\eta| <$

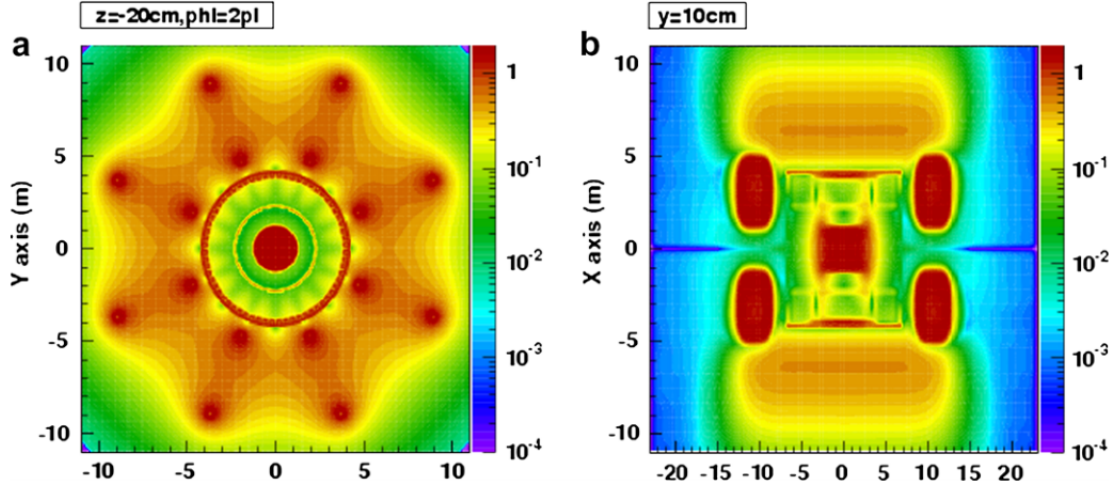


Figure 3.3: The shape of the magnetic field within the ATLAS detector [22].

2.5 and consists of the Pixel Detector, Semiconductor Tracker (SCT), and the Transition Radiation Tracker (TRT). These components can be seen in Figure 3.4.

Both the pixel detector and SCT consist of thousands of silicon sensors. The pixel detector consists of 1744 silicon wafers (each $250\text{ }\mu\text{m}$ thick), and the SCT of 15912 silicon wafers (each $28515\text{ }\mu\text{m}$ thick). The charged particles that pass through the pixel detector and SCT ionise within the submodules silicon semiconductors, freeing electrons from atoms within the silicon and creating ion-electron pairs. By interpreting the resultant signal created at the points within these wafers that these ion-electron pairs are created, the path of the charged particles that pass through the inner detector can be measured [19–21].

The inner detector performs several crucial functions within ATLAS: By performing measurements of charged particles that pass through the inner detector as their paths are bent by the magnet system, the inner detector can perform preliminary momentum measurements and track the paths of these charged particles throughout ATLAS. The measurements of momentum performed by the inner detector are supplemented by readings from other detector subsystems (such as energy deposits in the calorimeters), however the inner detector performs the most precise measurement of muon momentum. The paths measured by the inner detector provide excellent measurements of the tracks of charged particles, and are crucial for reconstructing events within ATLAS as they allow the detector triggers to correlate particle tracks to hits in other detector systems. By mapping hits in other detector subsystems with the paths tracked by the inner detector, it is possible to identify the kinematics and flavour of each particle travelling through ATLAS in order to fully describe each event. The inner detector is also responsible for identifying the main interaction point of each collision, by tracing the particle tracks back to the point where they originate.

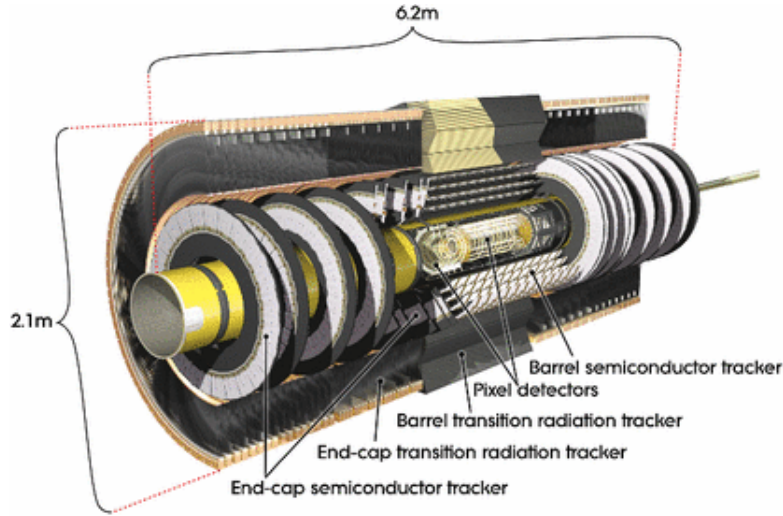


Figure 3.4: A figure showing the layout of the inner detector within ATLAS [21].

The number of particle tracks that occur within each event is very high, and in order to perform these measurements the inner detector must have a very high spatial resolution. The pixel detector and SCT have spatial resolutions of $12\mu\text{m}$ and $16\mu\text{m}$ respectively, which is essential to allow the detector to discern between the tracks of charged particles within the inner detector. The large number of events that occur within ATLAS every second can only be measured if the detector is able to accurately measure each involved particle, hence being able to distinguish each events tracks and collision points is essential to all measurements performed by ATLAS.

As charged particles pass through the TRT, they pass through drift tubes filled with a mixture of xenon, carbon dioxide, and oxygen gas. The charged particles emit transition radiation as they pass from the detector material into the gas, and also ionise the gas as they travel through it. The number of photons produced via transition radiation and electrons produced from EM-ionisation can be used to help distinguish between charged particles such as electrons and pions. By observing which of the drift tubes detected a signal, the TRT can supplement the measurement of the path of the charged particle performed by the pixel detector and SCT.

3.2.3 Calorimeter System

Two different calorimeters surround the inner detector and solenoid magnet to continue the measurements of particles travelling through ATLAS: the Electromagnetic Calorimeter and Hadronic Calorimeter (each of which consists of multiple pieces). The ATLAS calorimeters are sampling calorimeters, meaning that they work via a combination of absorber (or sampling) materials which cause an interaction within the module, and an

active material which produces a signal which is interpreted by ATLAS. The electromagnetic calorimeter consists of lead absorbers with a liquid argon (LAr) activate material, and the hadronic calorimeter consists of steel absorbers with scintillators as the active material. The layout of the calorimeter system can be seen in Figure 3.5.

By working in tandem, the two calorimeters perform measurements of the energy deposited by the travelling particles, regardless of whether the particles are charged or neutral. Naturally, the electromagnetic calorimeter focuses on absorbing the energy produced in electromagnetic showers, and the Hadronic calorimeter absorbs energy from hadronic showers. Both calorimeters surround the beam pipe, fully covering the azimuthal angle ϕ . Each calorimeter system is a combined effort from several pieces in order to cover a large range of $|\eta| < 4.9$.

In order to allow ATLAS to operate at maximum efficiency, incoming particles that cause electromagnetic and hadronic showers need to be fully contained within the calorimeters. This ensures that ATLAS can study the full shower, and prevents particles other than muons from penetrating through to the muon system. This is achieved by constructing the calorimeters to be an appropriate depth: the EM calorimeter is designed to be between 24 and 27 radiation lengths (X_0) deep, and the hadronic calorimeter is designed to be 10 nuclear interaction lengths (λ) thick. X_0 and λ represent the differing manners in which EM and hadronic particles lose energy, and for each unit one radiation/interaction length is the distance at which a travelling particle decreases to $1/e$ of its original energy.

The electromagnetic calorimeter consists of three parts: a barrel calorimeter and two end-cap calorimeters, with the barrel calorimeter covering $0 < |\eta| < 1.475$ and the end-cap calorimeters covering $1.375 < |\eta| < 3.2$. All of these calorimeters follow the geometry of an accordion, allowing full coverage of ϕ within the EM calorimeter without any spaces [19–21].

EM particles passing through the EM calorimeter interact with lead absorbers, creating a shower of lower energy particles. The incoming particles produce photons via the bremsstrahlung process (or other means such as a pion producing two photons), which then produce additional electrons via pair production. This alternating process of emitting photons which then produce electrons continues until the total energy of the shower is below that required for pair production to occur. Muons are capable of radiating photons as they pass through the EM calorimeter, which may produce additional secondary objects themselves. Typically these jets will be far less energetic than those produced by incoming electrons and photons, as photons radiated by muons carry only a small portion of the incident muons energy.

The EM calorimeter is fine-granulated, so that the calorimeter can reconstruct each showering particle. EM showers can easily have many simultaneous interactions (such as a pion decaying into two photons within proximity of an additional photon), and it is important to be able to distinguish between these occurrences for a detailed analysis.

Once these incident particles have lost enough energy to be beneath the energy require-

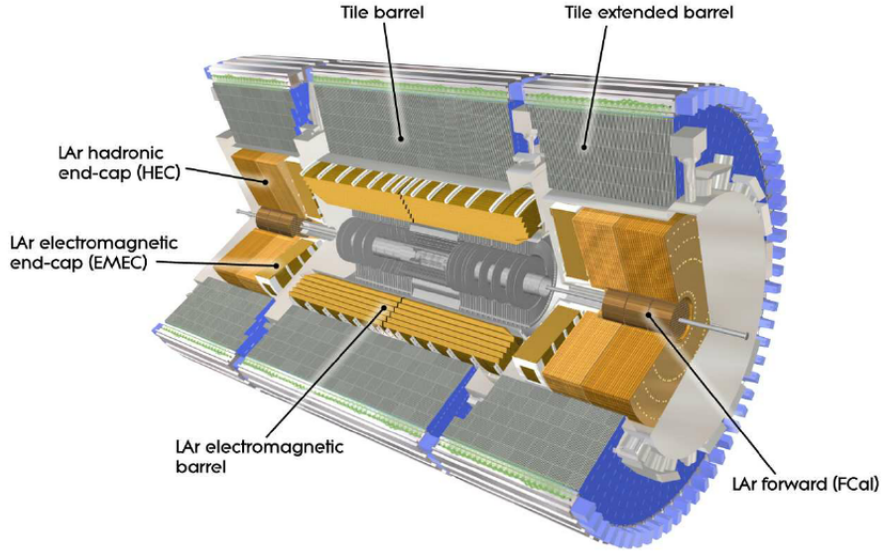


Figure 3.5: A figure displaying the arrangement of the electromagnetic and hadronic calorimeters within the ATLAS detector [21].

ment to produce an EM shower, energy loss mainly occurs by ionisation of the LAr within the EM calorimeter which frees additional electrons. The electrons produced within the LAr are attracted toward a copper electrode where they are interpreted into an electronic signal which reveals the amount of energy deposited by the original incident EM particle. Within the EM calorimeter, the thickness is $> 22 X_0$ thick in the barrel calorimeters and $> 24 X_0$ in the end-cap calorimeters.

The hadronic calorimeter is similarly consisting of three distinct parts: the hadronic tile calorimeter, LAr forward calorimeter (FCal), and the LAr hadronic end-caps (HEC). One large central barrel cylinder and two smaller extended barrel cylinders make up the tile calorimeter - a system of alternating steel absorbers and scintillating plates.

Travelling hadrons interact with the nuclei of the steel absorbers, producing additional particles. These particles then continue to interact, producing large showers of interactions. As these showers continue into the hadronic calorimeter, charged particles produce photons within the scintillating material. The photons emitted are carried to photomultiplier tubes via wavelength shifting fibres, where the photomultiplier tubes (PMTs) convert the photons into an electronic signal. By measuring the intensity of the light that creates the electronic signal, the energy deposited by the travelling hadron can be measured. The barrel tile calorimeter has a total thickness of 9.7λ for the combination of both the central barrel cylinder and extended barrel cylinders [19–21].

In order to be able to accurately measure the energy of incoming particles, the barrel calorimeter is required to have a high energy resolution (σ/E). In an event where energy is

deposited within a calorimeter, a calorimeter with high energy efficiency is better equipped to reconstruct the energy of the original event (and therefore high energy resolution was an important factor considered during the design of ATLAS). Using electron test beam measurements, the energy resolution of the EM barrel calorimeter was found to be $\sigma/E = 10\%/\sqrt{E} \oplus 2\%$ (where the simple \oplus represents a quadratic sum) [23].

In addition to the barrel tile calorimeter which covers a range of $0 < |\eta| < 1.0$ are the HEC and the FCal, which maximise the coverage of the calorimeters. The FCal is positioned in the very far forward and backward regions of $3.1 < |\eta| < 4.9$. The FCal consists of three modules, each containing a layer of a metal absorber and electrodes, plus LAr as the active detecting material. The first module is made of copper in order to allow electromagnetic measurements, and the other two layers are made of tungsten to allow measurements of hadronic interactions in the same method as the tile calorimeter. The total depth of the FCal is 10 interaction lengths.

The HEC overlaps with the tile calorimeter and the FCal in order to ensure full coverage. The HEC uses copper as its absorber and LAr as its active material, covering a range of $1.5 < |\eta| < 3.2$. Together these three pieces form the hadronic calorimeter and cover the pseudorapidity range of $0 < |\eta| < 4.9$. In test beam studies, the energy resolution of hadrons in the tile calorimeter was measured to be $\sigma/E = 52.9\%/\sqrt{E} \oplus 5.7\%$ [24].

3.2.4 Muon System

The final ATLAS detector subsystem is the muon system which rests outside the calorimeter system and inner detector. The muon systems role is to measure the path and momentum of muons in the pseudorapidity range of $|\eta| < 2.7$. The measurements in this region are dependent upon the toroidal magnets, which allow the tracks of charged particles able to penetrate the other detector systems to be measured. The barrel toroid provides the magnetic field in the region $|\eta| < 1.4$, the end-cap toroids provide the field in the region $1.6 < |\eta| < 2.7$, and the two work in tandem to produce the field in the transition region of $1.4 < |\eta| < 1.6$.

The bending of the muon tracks allows for measurements to be made in a similar fashion as to within the inner detector, and this is coupled with additional measurements from four components: precision measurements from monitored drift tubes (MDT) and cathode strip chambers (CSC), and trigger measurements from resistive plate chambers (RPC) and thin gap chambers (TGC).

The CSCs are located in the forward regions of $2 < |\eta| < 2.7$, as they are capable of dealing with the highest particle fluxes of up to 1000 Hzcm^{-2} . The MDTs are located cover the region $|\eta| < 2.7$ and consist of layers of drift tubes: cylinders containing a mixture of argon and carbon dioxide gas, with a wire at the centre. Muons that travel through the drift tubes ionise the gas and produce electrons and ions which drift to the wire and edge of the drift tube respectively, and are interpreted as an electronic signal. By

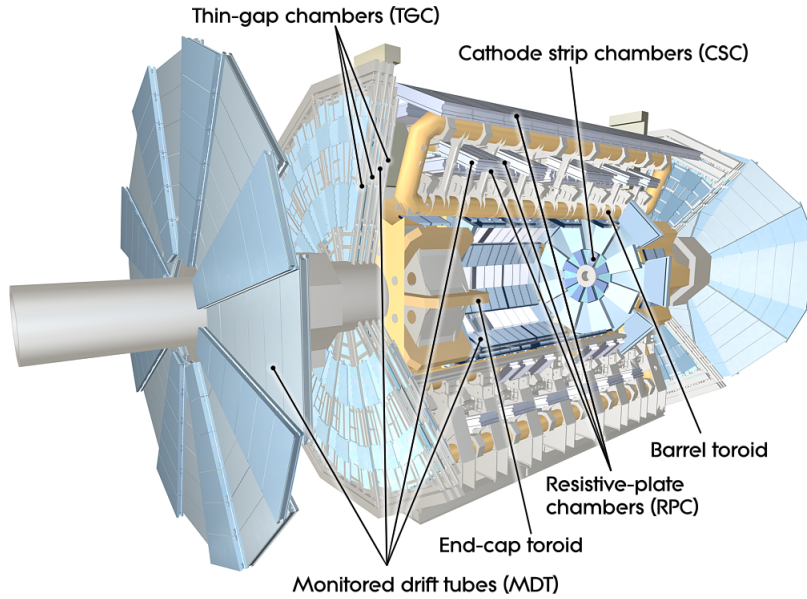


Figure 3.6: A figure showing the position of the individual muon systems within ATLAS [21].

observing the amount of ionisation, particle drift time, and the time and position of each emitted signal, the momentum of the travelling muon can be measured. The layout of the muon system can be seen in Figure 3.6.

The RPCs and TGCs serve as fast trigger chambers, able to provide track information approximately 10ns after a particle penetrates. The RPCs are located in the barrel covering the range $|\eta| < 1.05$, and the TGCs in the end-cap covering the region $1.05 < |\eta| < 2.4$. While the CSCs and MDTs record precision measurements regarding the incident muons, the RPCs and TGCs are utilised for providing information to the trigger systems.

The RPCs are gaseous parallel electrode-plate detectors consisting of two resistive plates separated by a 2mm gas gap: incoming muons are deflected towards the anode of the RPC allowing for a signal readout. TPCs are multi-wire proportional chambers arranged into layers positioned around the MDTs and in front of the most inward positioned tracking layer. As incident muons penetrate the sub layers within the TPCs, a signal is emitted if a muon is detected in multiple layers of the detector. The time and position of where this signal originates corresponds to a muon hit, and aids the trigger system in identifying muon events [19–21].

3.2.5 Trigger System

The trigger systems function is to manage the enormous number of collisions that occur within ATLAS every second, identifying events that correspond to the expected standards of ATLAS, and ignoring those that do not. This operation is performed by a combination of a hardware based Level 1 (L1) trigger and a software based High Level Trigger (HLT).

The L1 trigger uses information from the calorimeters and muon system to identify regions of interest within the recorded data, and performs the first classification of the data recorded, before passing events are sent to the HLT. This operation takes place within 2.5s, and reduces the event rate from 40MHz to less than 75kHz (although it is still possible to operate with up to 100kHz output rate from the L1 trigger).

The HLT runs on a dedicated server farm, and uses high speed algorithms to further refine events in the region of interest that pass the L1 trigger. The HLT reduces the event rate further to 1kHz, processing each event in an average of 0.2s.

References

- [1] P. Nason, S. Dawson, and R. Keith Ellis. The One Particle Inclusive Differential Cross-Section for Heavy Quark Production in Hadronic Collisions. *Nucl. Phys.*, B327:49–92, 1989. doi: 10.1016/0550-3213(90)90180-L, 10.1016/0550-3213(89)90286-1. [Erratum: Nucl. Phys.B335,260(1990)].
- [2] John M. Campbell, R. Keith Ellis, F. Maltoni, and S. Willenbrock. Associated production of a Z Boson and a single heavy quark jet. *Phys. Rev.*, D69:074021, 2004. doi: 10.1103/PhysRevD.69.074021.
- [3] John M. Campbell, R. Keith Ellis, F. Maltoni, and S. Willenbrock. Production of a Z boson and two jets with one heavy-quark tag. *Phys. Rev.*, D73:054007, 2006. doi: 10.1103/PhysRevD.77.019903, 10.1103/PhysRevD.73.054007. [Erratum: Phys. Rev.D77,019903(2008)].
- [4] Fernando Febres Cordero, L. Reina, and D. Wackeroth. W- and Z-boson production with a massive bottom-quark pair at the Large Hadron Collider. *Phys. Rev.*, D80:034015, 2009. doi: 10.1103/PhysRevD.80.034015.
- [5] Georges Aad et al. Measurement of differential production cross-sections for a Z boson in association with b -jets in 7 TeV proton-proton collisions with the ATLAS detector. *JHEP*, 10:141, 2014. doi: 10.1007/JHEP10(2014)141.
- [6] Serguei Chatrchyan et al. Inclusive b -jet production in pp collisions at $\sqrt{s} = 7$ TeV. *JHEP*, 04:084, 2012. doi: 10.1007/JHEP04(2012)084.

- [7] M. Tanabashi, K. Hagiwara, K. Hikasa, K. Nakamura, Y. Sumino, F. Takahashi, J. Tanaka, K. Agashe, G. Aielli, C. Amsler, M. Antonelli, D. M. Asner, H. Baer, Sw. Banerjee, R. M. Barnett, T. Basaglia, C. W. Bauer, J. J. Beatty, V. I. Belousov, J. Beringer, S. Bethke, A. Bettini, H. Bichsel, O. Biebel, K. M. Black, E. Blucher, O. Buchmuller, V. Burkert, M. A. Bychkov, R. N. Cahn, M. Carena, A. Ceccucci, A. Cerri, D. Chakraborty, M.-C. Chen, R. S. Chivukula, G. Cowan, O. Dahl, G. D'Ambrosio, T. Damour, D. de Florian, A. de Gouvêa, T. DeGrand, P. de Jong, G. Dissertori, B. A. Dobrescu, M. D'Onofrio, M. Doser, M. Drees, H. K. Dreiner, D. A. Dwyer, P. Eerola, S. Eidelman, J. Ellis, J. Erler, V. V. Ezhela, W. Fetscher, B. D. Fields, R. Firestone, B. Foster, A. Freitas, H. Gallagher, L. Garren, H.-J. Gerber, G. Gerbier, T. Gershon, Y. Gershtein, T. Gherghetta, A. A. Godizov, M. Goodman, C. Grab, A. V. Gritsan, C. Grojean, D. E. Groom, M. Grünewald, A. Gurtu, T. Gutsche, H. E. Haber, C. Hanhart, S. Hashimoto, Y. Hayato, K. G. Hayes, A. Hebecker, S. Heinemeyer, B. Heltsley, J. J. Hernández-Rey, J. Hisano, A. Höcker, J. Holder, A. Holtkamp, T. Hyodo, K. D. Irwin, K. F. Johnson, M. Kado, M. Karliner, U. F. Katz, S. R. Klein, E. Klempt, R. V. Kowalewski, F. Krauss, M. Kreps, B. Krusche, Yu. V. Kuyanov, Y. Kwon, O. Lahav, J. Laiho, J. Lesgourgues, A. Liddle, Z. Ligeti, C.-J. Lin, C. Lippmann, T. M. Liss, L. Littenberg, K. S. Lugovsky, S. B. Lugovsky, A. Lusiani, Y. Makida, F. Maltoni, T. Mannel, A. V. Manohar, W. J. Marciano, A. D. Martin, A. Masoni, J. Matthews, U.-G. Meißner, D. Milstead, R. E. Mitchell, K. Mönig, P. Molaro, F. Moortgat, M. Moskvic, H. Murayama, M. Narain, P. Nason, S. Navas, M. Neubert, P. Nevski, Y. Nir, K. A. Olive, S. Pagan Griso, J. Parsons, C. Patrignani, J. A. Peacock, M. Pennington, S. T. Petcov, V. A. Petrov, E. Pianori, A. Piepke, A. Pomarol, A. Quadt, J. Rademacker, G. Raffelt, B. N. Ratcliff, P. Richardson, A. Ringwald, S. Roesler, S. Rolli, A. Romaniouk, L. J. Rosenberg, J. L. Rosner, G. Rybka, R. A. Ryutin, C. T. Sachrajda, Y. Sakai, G. P. Salam, S. Sarkar, F. Sauli, O. Schneider, K. Scholberg, A. J. Schwartz, D. Scott, V. Sharma, S. R. Sharpe, T. Shutt, M. Silari, T. Sjöstrand, P. Skands, T. Skwarnicki, J. G. Smith, G. F. Smoot, S. Spanier, H. Spieler, C. Spiering, A. Stahl, S. L. Stone, T. Sumiyoshi, M. J. Syphers, K. Terashi, J. Terning, U. Thoma, R. S. Thorne, L. Tiator, M. Titov, N. P. Tkachenko, N. A. Törnqvist, D. R. Tovey, G. Valencia, R. Van de Water, N. Varelas, G. Venanzoni, L. Verde, M. G. Vincet, P. Vogel, A. Vogt, S. P. Wakely, W. Walkowiak, C. W. Walter, D. Wands, D. R. Ward, M. O. Wascko, G. Weiglein, D. H. Weinberg, E. J. Weinberg, M. White, L. R. Wiencke, S. Willocq, C. G. Wohl, J. Womersley, C. L. Woody, R. L. Workman, W.-M. Yao, G. P. Zeller, O. V. Zenin, R.-Y. Zhu, S.-L. Zhu, F. Zimmermann, P. A. Zyla, J. Anderson, L. Fuller, V. S. Lugovsky, and P. Schaffner. Review of particle physics. *Phys. Rev. D*, 98:030001, Aug 2018. doi: 10.1103/PhysRevD.98.030001. URL <https://link.aps.org/doi/10.1103/PhysRevD.98.030001>.
- [8] Fabio Maltoni, Giovanni Ridolfi, and Maria Ubiali. b-initiated processes at the LHC: a reappraisal. *JHEP*, 07:022, 2012. doi: 10.1007/JHEP04(2013)095,

- 10.1007/JHEP07(2012)022. [Erratum: JHEP04,095(2013)].
- [9] Juan Rojo. PDF4LHC recommendations for Run II. *PoS*, DIS2016:018, 2016.
 - [10] Georges Aad et al. (ATLAS Collaboration). Observation of a new particle in the search for the Standard Model Higgs boson with the ATLAS detector at the LHC. *Phys. Lett.*, B716:1–29, 2012. doi: 10.1016/j.physletb.2012.08.020.
 - [11] Serguei Chatrchyan et al. (CMS Collaboration). Observation of a new boson at a mass of 125 GeV with the CMS experiment at the LHC. *Phys. Lett.*, B716:30–61, 2012. doi: 10.1016/j.physletb.2012.08.021.
 - [12] Guido Altarelli. A QCD primer. *AIP Conf. Proc.*, 631(1):70, 2002. doi: 10.1063/1.1513677.
 - [13] F. Englert and R. Brout. Broken symmetry and the mass of gauge vector mesons. *Phys. Rev. Lett.*, 13:321–323, Aug 1964. doi: 10.1103/PhysRevLett.13.321. URL <https://link.aps.org/doi/10.1103/PhysRevLett.13.321>.
 - [14] Peter W. Higgs. Broken symmetries and the masses of gauge bosons. *Phys. Rev. Lett.*, 13:508–509, Oct 1964. doi: 10.1103/PhysRevLett.13.508. URL <https://link.aps.org/doi/10.1103/PhysRevLett.13.508>.
 - [15] Sidney D. Drell and Tung-Mow Yan. Massive lepton-pair production in hadron-hadron collisions at high energies. *Phys. Rev. Lett.*, 25:316–320, Aug 1970. doi: 10.1103/PhysRevLett.25.316. URL <https://link.aps.org/doi/10.1103/PhysRevLett.25.316>.
 - [16] A. D. Martin, W. J. Stirling, R. S. Thorne, and G. Watt. Parton distributions for the LHC. *Eur. Phys. J.*, C63:189–285, 2009. doi: 10.1140/epjc/s10052-009-1072-5.
 - [17] Lyndon Evans and Philip Bryant. LHC Machine. *JINST*, 3:S08001, 2008. doi: 10.1088/1748-0221/3/08/S08001.
 - [18] Christiane Lefvre. The CERN accelerator complex. Complexe des accélérateurs du CERN. Dec 2008. URL <https://cds.cern.ch/record/1260465>.
 - [19] A. Airapetian et al. ATLAS: Detector and physics performance technical design report. Volume 1. 1999.
 - [20] A. Airapetian et al. ATLAS: Detector and physics performance technical design report. Volume 2. 1999.
 - [21] G. Aad et al. The ATLAS Experiment at the CERN Large Hadron Collider. *JINST*, 3:S08003, 2008. doi: 10.1088/1748-0221/3/08/S08003.

- [22] H.H.J. ten Kate. The atlas superconducting magnet system at the large hadron collider. *Physica C: Superconductivity*, 468(15):2137 – 2142, 2008. ISSN 0921-4534. doi: <https://doi.org/10.1016/j.physc.2008.05.146>. URL <http://www.sciencedirect.com/science/article/pii/S0921453408004541>. Proceedings of the 20th International Symposium on Superconductivity (ISS 2007).
- [23] M. Aharrouche and ATLAS Electromagnetic Barrel Calorimeter Collaboration. Energy linearity and resolution of the atlas electromagnetic barrel calorimeter in an electron test-beam. 2006. doi: 10.1016/j.nima.2006.07.053.
- [24] P. Adragna et al. Testbeam studies of production modules of the ATLAS tile calorimeter. *Nucl. Instrum. Meth.*, A606:362–394, 2009. doi: 10.1016/j.nima.2009.04.009.

November 2019 - January 2020: Framework Development and Validation

The multiple frameworks in the Z+hf analysis group currently show promise, but are not yet ready for full analysis. During this time period, it would be ideal to achieve the following goals:

- Implement systematic uncertainties
 - Currently the ZHFReader code has functionality for the systematics, but they do not appear to function correctly.
- Validate between the frameworks
 - This requires participation within the analysis group and is not fully attainable by working alone, however there are some steps that could already be taken to prepare for this stage such as production of lists of event numbers.

February 2020 - April 2020: Production of top and multijet enriched control regions

Measurements of prevalent backgrounds can be performed in order to reduce uncertainties before unfolding, or to even to avoid propagating negligible backgrounds through the entire analysis. During this time period, it would be ideal to achieve the following goals:

- Create a multijet enriched control region to enrich multijet event numbers by deliberately requiring the presence of multijet background events (for example by requiring two same sign muons as opposed to two opposite sign muons).
- Create a top control region to enrich top event numbers by treating $emum$ events as a signal source as opposed to ee or $mumu$ events.
- Analyse these control regions and their systematic uncertainties in order to obtain accurate event numbers and neglecting to propagate these backgrounds through the analysis if these backgrounds are negligible.

May 2020 - July 2020: Flavour fit

In the same way that top and multijet control regions can be used to perform accurate measurements of these backgrounds, a flavour fit can be used to distinguish between the Z + light, Z + charm, and Z + bottom backgrounds. This is especially important for the Z+b process, as Z + light and Z + charm are two of the largest background contributors. During this time period, it would be ideal to perform this fit for both the Z+b and Z+bb processes. During this time period, it would be ideal to achieve the following goal:

- Perform an accurate flavour fit for both the Z+b and Z+bb channels

August - October 2020: Unfolding and generator comparisons

Unfolding is the crucial step that allows an analysis taking place at detector level to be transposed to particle level in order to obtain meaningful results. Prior to unfolding, the best possible modelling of the obtained data can be found by performing comparisons between multiple varieties of monte carlo generator. More MC samples from a greater variety of generators can be obtained by making the analysis appealing to PMG members. During this time period, it would be ideal to achieve the following goals:

- Reproduce existing work using a variety of different MC generators
- Unfold the analysis to a high degree of accuracy